Designing Magnetic Properties in CrSBr through Hydrostatic Pressure and Ligand Substitution

Evan J. Telford, Daniel G. Chica, Michael E. Ziebel, Kaichen Xie, Nicholas S. Manganaro, Chun-Ying Huang, Jordan Cox, Avalon H. Dismukes, Xiaoyang Zhu, James P. S. Walsh, Ting Cao, Cory R. Dean, and Xavier Roy*

Magnetic van der Waals (vdW) materials are a promising platform for producing atomically thin spintronic and optoelectronic devices. The A-type antiferromagnet CrSBr has emerged as a particularly exciting material due to its high magnetic ordering temperature, semiconducting electrical properties, and enhanced chemical stability compared to other vdW magnets. Exploring mechanisms to tune its magnetic properties will facilitate the development of nanoscale devices based on vdW materials with designer magnetic properties. Here it is investigated how the magnetic properties of CrSBr change under pressure and ligand substitution. Pressure compresses the unit cell, increasing the interlayer exchange energy while lowering the Néel temperature. Ligand substitution, realized synthetically through Cl alloying, anisotropically compresses the unit cell and suppresses the Cr-halogen covalency, reducing the magnetocrystalline anisotropy energy and decreasing the Néel temperature. A detailed structural analysis combined with first-principles calculations reveals that alterations in the magnetic properties are intricately related to changes in direct Cr–Cr exchange interactions and the Cr–anion superexchange pathways. Further, it is demonstrated that Cl alloying enables chemical tuning of the interlayer coupling from antiferromagnetic to ferromagnetic, which is unique among known two-dimensional magnets.

1. Introduction

The discovery of two-dimensional (2D) magnets,[1] prepared by mechanical exfoliation of bulk van der Waals (vdW) materials, provides an ideal platform to understand and ultimately control 2D magnetism, fueling opportunities for atomically thin spintronic[2] and magneto-optic devices.[3] Among the growing number of 2D vdW magnets, including binary metal halides[4] and chalcogenides,[5] MXenes,[6] and transition metal ternary compounds,[7] the vdW A-type anti-ferromagnet CrSBr has emerged as a particularly exciting material boasting a high Néel temperature $T_N = 132$ K, stability under ambient conditions,[7e,8] and functional semiconducting transport properties.[8,9] Furthermore, CrSBr manifests a uniquely strong coupling between magnetism and electronic,[8,9] optical,[7e,10] and structural properties,[11] as well as tunable coupling between magnons and excitons.[12] Consequently, developing routes to modify the bulk magnetic properties of CrSBr could unlock new magneto-optical, magneto-electric, magneto-elastic, and quantum transduction phenomena that can be functionalized in the next generation of nanoscale spintronic and optoelectronic devices. Recent experiments demonstrated that uniaxial strain on thin flakes of CrSBr changed the magnetic ground state from antiferromagnetic (AFM) to ferromagnetic (FM) due to a change in the sign of

E. J. Telford, D. G. Chica, M. E. Ziebel, C.-Y. Huang, J. Cox,
A. H. Dismukes, X. Zhu, X. Roy
Department of Chemistry
Columbia University
New York, NY 10027, USA
E-mail: xr2114@columbia.edu

E. J. Telford, M. E. Ziebel, C. R. Dean
Department of Physics
Columbia University
New York, NY 10027, USA

K. Xie, T. Cao
Department of Materials Science and Engineering
University of Washington
Seattle, WA 98195, USA

N. S. Manganaro, J. P. S. Walsh
Department of Chemistry
University of Massachusetts Amherst
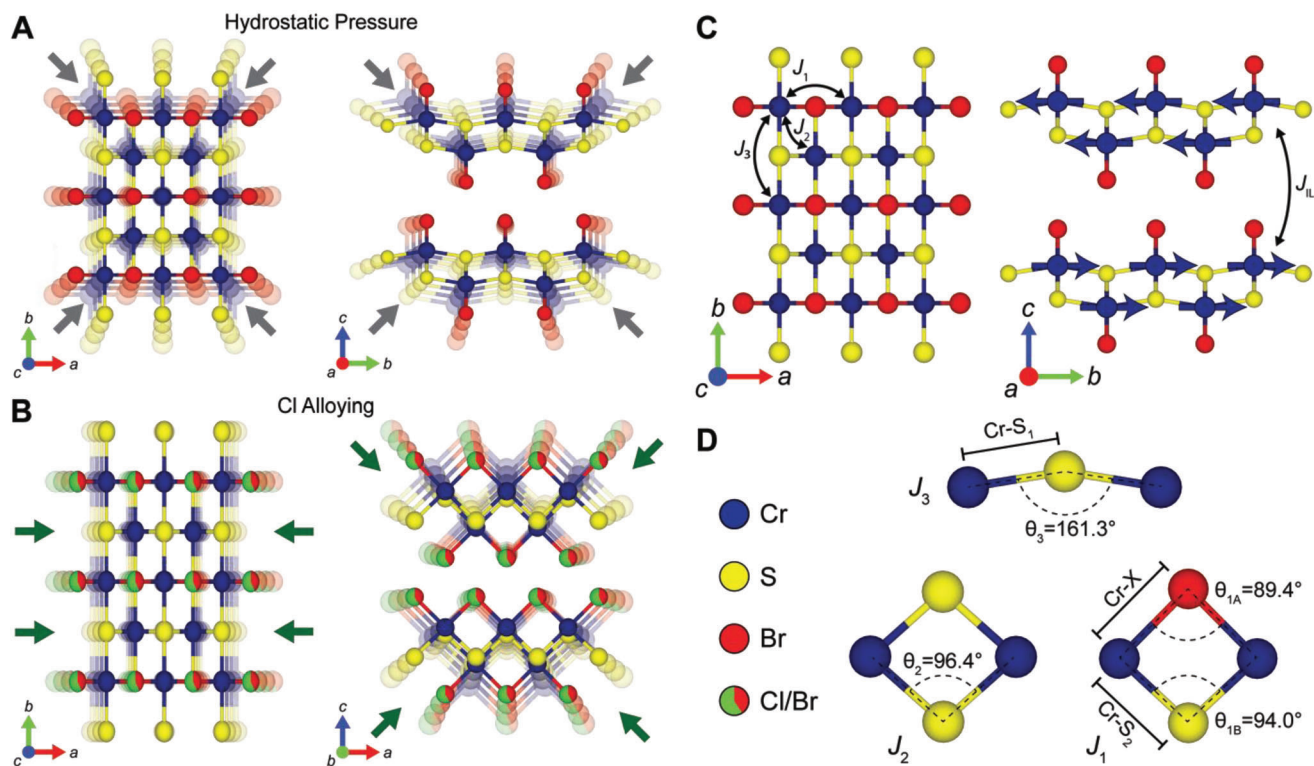Amherst, MA 01003, USA

Figure 1. Structure and magnetic coupling of CrSBr under pressure and Cl alloying. A) Schematic depicting the effect of pressure on the crystal structure of CrSBr as viewed along the c-axis (left) and a-axis (right). The dark gray arrows denote the qualitative direction of the unit-cell changes. B) Schematic depicting the effect of Cl alloying on the crystal structure of CrSBr$_{1-x}$Cl$_x$ as viewed along the c-axis (left) and b-axis (right). Dark green arrows denote the qualitative direction of the unit-cell changes. C) Crystal structure of CrSBr as viewed along the c-axis (left) and a-axis (right). Double-ended black arrows denote the direction of the relevant magnetic couplings. Dark blue arrows denote the direction of Cr^{3+} moments in the AFM state. D) Schematic of the superexchange pathways for the three largest intraplanar FM couplings in CrSBr. The corresponding bonds and bond angles contributing to the superexchange interactions are labeled.

the interlayer coupling.[11] However, there have been no experimental investigations of strategies to tune the *intralayer* coupling in CrSBr, which is expected to more strongly affect its magnetic properties. Understanding how structural and electronic modifications to CrSBr affect these intralayer magnetic properties will enable the engineering of new materials in this class of transition-metal ternary compounds with designer magneto-electronic and magneto-optical properties.

In this work, we uncover how physical and chemical modifications of the CrSBr structure affect the magnetic properties through combined magnetic, structural, and computational analysis. We find that compression of the lattice under pressure (**Figure 1**A) reduces T_N through suppression of intralayer FM interactions and increases all axial saturation fields due to an increase in interlayer exchange energy. Upon Cl alloying, the combined effects of anisotropic lattice compression (Figure 1B) and reduced Cr–halogen covalency lead to an even larger decrease in T_N and a *decrease* in all axial saturation fields due to the combined decrease of interlayer exchange energy and magnetic anisotropy. In both cases, the reduced ordering temperature comes from suppressed intralayer FM superexchange interactions, highlighting the delicate balance between Cr–Cr direct exchange and Cr–anion superexchange pathways. At the highest accessible Cl content, the suppressed in-plane magnetic anisotropy results in a

glassy magnetic ground state, hosting competing FM and AFM interlayer interactions, which could prove useful for interrogating phase transitions between FM and AFM states with external stimuli. Together, these results reveal a rich magnetic phase space within the CrSBr family, motivating further exploration of pre- and post-synthetic mechanisms that could, for example, grant access to 2D-XY-like regimes or *increase* the magnetic ordering temperature.

The structure of a vdW CrSBr layer consists of two buckled rectangular planes of CrS fused together, with both surfaces capped by Br atoms (Figure 1C). Stacking of the layers along the c-axis produces an orthorhombic structure with the space group $Pmmn$.[8,13] The primary magnetic couplings consist of three intralayer FM superexchange interactions (denoted J_1, J_2, and J_3) mediated by intralayer Cr—S—Cr and Cr—Br—Cr bonds (Figure 1D).[14] The interlayer AFM super-superexchange coupling (J_{IL}) is mediated by Cr–Br–Br–Cr interactions between the sheets (Figure 1C).[7e,10,14g,15] The strong intralayer coupling gives rise to short-range FM correlations below a characteristic temperature ($T_c \approx 160$ K),[7e,8,14f,g] while the weaker interlayer exchange (Table S1, Supporting Information) induces long-range A-type AFM order below $T_N = 132$ K.[14g] In the magnetically ordered state, each layer orders ferromagnetically with adjacent layers aligned antiferromagnetically along the stacking direction

**ADVANCED
SCIENCE NEWS**

www.advancedsciencenews.com

**ADVANCED
PHYSICS
RESEARCH**

Open Access

www.advphysicsres.com

(Figure 1C).[8,13a,14f,g] CrSBr exhibits uniaxial magnetic anisotropy along the b-axis, originating from anisotropic exchange interactions mediated by the surface-capping Br.[14f,16]

2. Results and Discussion

2.1. CrSBr Under Pressure

While intralayer superexchange interactions in CrSBr are FM, analogous interactions in the isostructural compounds VOCl,[17] CrOCl,[18] and FeOCl[19] are AFM, suggesting that the sign of magnetic exchange in this family of materials may be highly sensitive to Cr—halogen—Cr and Cr—chalcogen—Cr bond angles. With this in mind, we chose hydrostatic pressure (P) as an initial route to modify the magnetic properties of CrSBr, as pressure provides a medium to modify the structure without changing chemical properties. For measurements of CrSBr under P, samples were prepared by grinding bulk single crystals in liquid nitrogen (see Experimental Section for details). The powder was then mixed with Daphne oil and loaded into a commercially available piston-cylinder pressure cell along with a small piece of Pb acting as a manometer (Figures S1–S3, Supporting Information and Experimental Section for details). We performed magnetic measurements on the randomly oriented powder as a function of temperature (T), magnetic field ($\mu_0 H$), and P.

Figure 2A presents the magnetic susceptibility (χ) of CrSBr versus T for various P up to 1.39 GPa. T_N manifests as a peak in χ versus T and is extracted numerically by finding the zero-crossings of dχ/dT (Figure S4, Supporting Information). The ambient-P $T_N = 135 \pm 3$ K is in agreement with previous reports.[7e,8,9,10,13a,14f,g,20] Upon the application of P, T_N decreases linearly at a rate of dT_N/d$P = -12.6 \pm 1.0$ K GPa^{-1} (inset of Figure 2A). Curie–Weiss analysis reveals that the Weiss temperature (θ_W) also decreases with increasing P, while the Curie constant (C) is independent of pressure (Figure S5, Supporting Information), indicating a weakening of the intralayer FM coupling strength with no change in the $S = {}^3/_2$ Cr^{3+} moments. Further measurements of χ versus T with a large applied $\mu_0 H = 3$ T (where all spins in the magnetic state are polarized along the field direction) (Figure S6, Supporting Information) show a paramagnetic(PM)-to-FM phase transition with a decreasing Curie temperature with increasing P, supporting the conclusion that increasing P weakens the intralayer FM coupling. In Figure 2B, we plot magnetization (M) versus $\mu_0 H$ with increasing P. Because the CrSBr samples were measured as a randomly oriented powder, we expect the M versus $\mu_0 H$ traces to be an average of the axial-oriented M versus $\mu_0 H$ traces (Figures S7 and S8, Supporting Information). At ambient P, M versus $\mu_0 H$ is approximately linear at low $\mu_0 H$ followed by a change in slope at $\mu_0 H = 0.28 \pm 0.05$ T (b-axis saturation field) and a subtle kink at $\mu_0 H = 0.46 \pm 0.05$ T (a-axis saturation field) followed by saturation at $\mu_0 H = 1.05 \pm 0.05$ T (c-axis saturation field). With increasing P, the low-field slope decreases, resulting in an increasing saturation magnetic field H_{SAT} (defined here as the $\mu_0 H$ at which $M = 0.9$ M_{SAT}). H_{SAT} increases at a rate of dH_{SAT}/d$P = 0.49 \pm 0.03$ T GPa^{-1} (inset of Figure 2B). For consistency, we repeated all measurements on a second CrSBr sample, which show quantitatively similar results (insets of Figure 2A,B and Figure S9, Supporting Information). We note that powder X-ray diffraction (PXRD) measurements showed no evidence of irreversible phase transitions after grinding or applying maximum P (Figure S10, Supporting Information).

To interpret the changes in magnetic properties of CrSBr under P, we measured the lattice parameters of CrSBr under P (Figures S11–S15, Supporting Information and Experimental Section for details) and performed complementary theoretical simulations to calculate both the relaxed structural parameters and magnetic properties of CrSBr under P (see Experimental Section for details). In Figure 2C, the experimental lattice parameters are plotted versus P. All lattice parameters decrease, with the most significant change along the c-axis. Our density functional theory calculations well-predict the experimental change in lattice parameters under P (Figure S12, Supporting Information) and find that, as the c-axis compresses, the corresponding interlayer AFM coupling drastically strengthens (by 340% at 1.5 GPa—inset of Figure 2D). From this, one might expect T_N to *increase* under P. However, all primary intralayer FM couplings weaken (J_1, J_2, and J_3—Figure 2D and Table S1, Supporting Information) and the magnitude of the strongest intralayer coupling, J_2, is more than 30 times that of J_{IL} for the entire P range, indicating that the *intralayer* magnetic exchange is the dominant contribution to the ordering temperature. The calculations fully support this conclusion, correctly predicting a decreasing T_N with increasing P (Figure 2E and Table S1, Supporting Information). Furthermore, the experimental observation of an increase in H_{SAT} with increasing P is explained by the strengthening of the interlayer AFM coupling, in agreement with our calculations (Figure 2E and Table S1, Figure S7, Supporting Information).

Using the computed high-pressure structures, we can begin to rationalize the observed magnetic properties and derive magneto-structural correlations for CrSBr. Looking first at the interlayer spacing, we find the theoretically predicted vdW gap decreases significantly ($\approx$10% at 1.5 GPa) with P, leading to an increase in Cr–Br–Br–Cr overlap and thus J_{IL} (Table S1, Supporting Information). The intralayer magnetic exchange is more complex. The intralayer exchange interactions in CrSBr represent a competition between FM superexchange interactions and weaker AFM direct exchange interactions. Changes in the superexchange interactions should be explained by the Goodenough–Kanamori–Anderson rules[21] for a Cr^{3+} ion. These would predict the strongest FM coupling for bond angles near 90° and the strongest AFM coupling for bond angles near 180°. In contrast, the strength of AFM direct exchange interactions increases exponentially as the distance between magnetic ions shrinks.

To understand the magnetic behavior of CrSBr under pressure, the effects of both direct exchange and superexchange must be considered. With increasing pressure, the magnitude of direct exchange should increase for J_1, J_2, and J_3, as all Cr–Cr distances ($d_{Cr–Cr}$) shrink (Table S1, Supporting Information). These changes should be most pronounced for J_1 and J_2, which have experimentally determined $d_{Cr–Cr}$ of $\approx$3.51 and $\approx$3.59 Å, respectively, whereas $d_{Cr–Cr}$ for J_3 is much larger ($\approx$4.76 Å). Because $d_{Cr–Cr}$ remains well outside the range of Cr—Cr bonding for all pressures studied here, we would expect the direct exchange interactions to remain small relative to superexchange interactions, which agrees with our experimental and computational data where the net intralayer coupling remains FM. However, the relative changes in the calculated exchange energies at 1.5 GPa
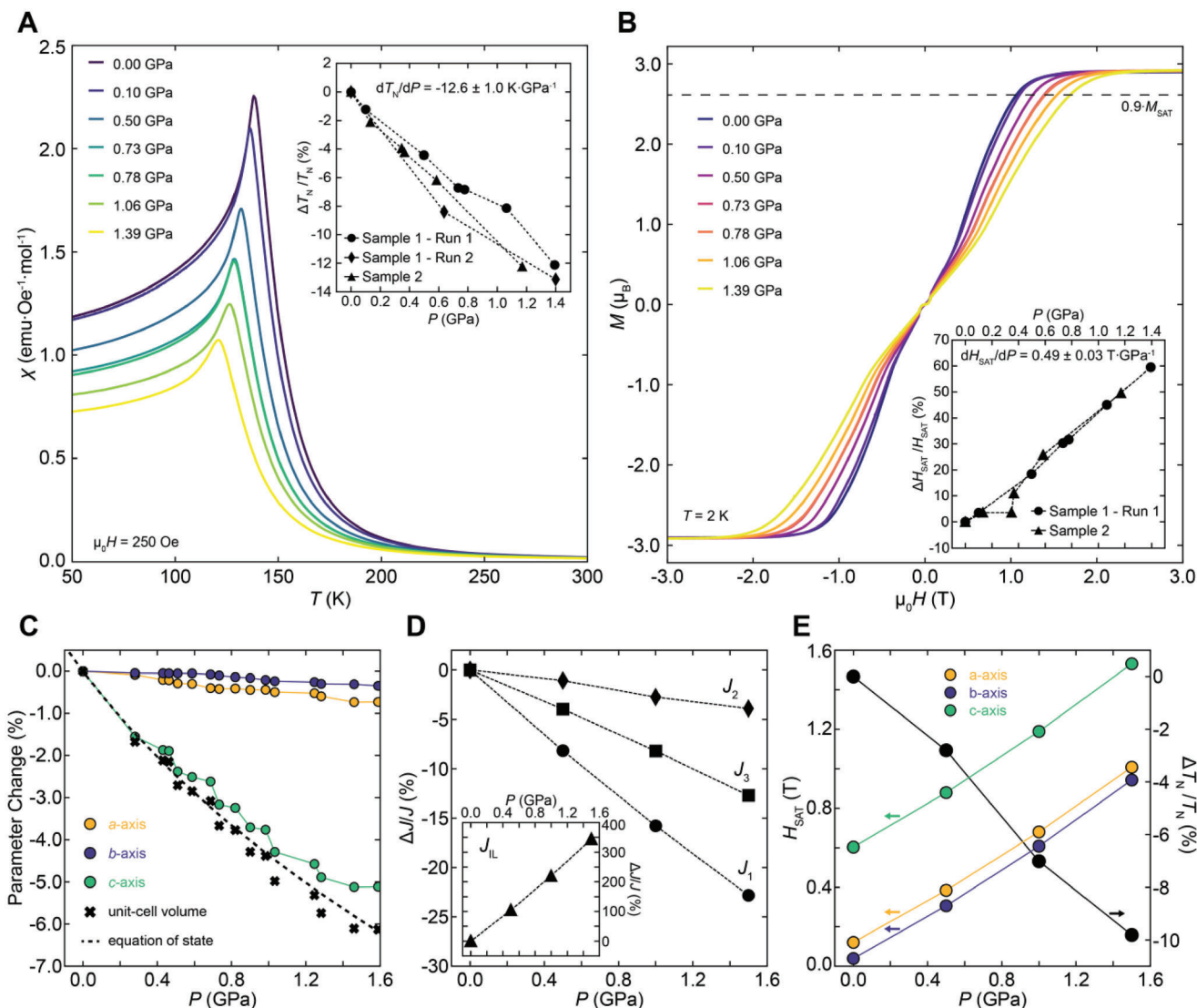
Figure 2. Magnetic properties of CrSBr under pressure. A) Zero-field-cooled χ versus T for various applied P. A measuring field of 250 Oe was used for all traces. Inset shows the extracted percentage change in T_N versus P for multiple measurement runs and different samples. The extracted slope of T_N versus P is given in the inset. B) M versus $\mu_0 H$ at 2 K for various P. $\mu_0 H$ is randomly oriented along all crystal axes. H_{SAT} is defined as the $\mu_0 H$ at which M is 90% of the saturation M (denoted by a black dashed line). Inset shows extracted H_{SAT} versus P with the extracted slope of H_{SAT} versus P. C) Percentage change in lattice constants and the unit-cell volume versus P, as determined by powder X-ray diffraction. The dashed black line is a fit to an equation of state (see Experimental Section for details). D) Calculated percentage change in intralayer magnetic couplings versus P. Inset: calculated percentage change in interlayer magnetic coupling (J_{IL}) versus P. E) Calculated H_{SAT} (left axis, orange, purple, and green dots) and T_N (right axis, solid black dots) versus P.

compared to ambient pressure ($\Delta J_1 \approx \Delta J_3 > \Delta J_2$) are inconsistent with the expectations for direct exchange alone ($\Delta J_1 \approx \Delta J_2 > \Delta J_3$), suggesting that superexchange pathways are also affected by lattice compression.

As noted above, changes in superexchange pathways under pressure should be most sensitive to changes in the Cr—S—Cr and Cr—Br—Cr bond angles. At 1.5 GPa, all of these angles are predicted to change by less than 1° compared to the relaxed ambient-pressure structure, suggesting that the modulation of the superexchange energies should be smaller or similar in magnitude to the changes in direct exchange (Table S1, Supporting Information). The largest change is observed in the Cr—S$_1$—Cr

bond angle (θ_3, Figure 1D), which increases toward 180°, enhancing the contribution of AFM exchange pathways and weakening the overall FM coupling (Table S1, Supporting Information). Consequently, both direct exchange and superexchange contributions contribute to the reduced magnitude of J_3 with increasing P. In contrast, for J_1 and J_2, all of the relevant Cr—S—Cr (θ_2 and θ_{1B}) and Cr—Br—Cr (θ_{1A}) (Figure 1D) bond angles trend toward 90° with increasing P (Table S1, Supporting Information), which should enhance the FM superexchange interactions. Since the changes in bond angles are relatively small, the magnitude of these effects is likely minimized and could be less than the corresponding increase in AFM direct Cr–Cr exchange. Collectively,

**ADVANCED
SCIENCE NEWS**

www.advancedsciencenews.com

**ADVANCED
PHYSICS
RESEARCH**
Open Access

www.advphysicsres.com

these results reiterate the balance between superexchange and direct exchange that must be considered when designing new materials in this family of ternary compounds.

2.2. Cl-Alloying of CrSBr

While these results motivate studies of the magnetic behavior of CrSBr at even higher pressures where larger bond angle changes may affect superexchange pathways more strongly, chemical modifications could more drastically alter superexchange pathways by both inducing larger structural changes than were obtained in the pressure range studied here and affecting the covalency of the Cr—halogen bonds. Specifically, we hypothesized that the substitution of Br with Cl could induce a large lattice compression, while simultaneously allowing us to study the effects of changing Cr–halogen covalency on the magnetic properties. Furthermore, theoretical studies on ligand engineering[22] and strain[15] on chromium chalcohalides demonstrate changes to the magnetic properties with these perturbations. To explore this hypothesis, we synthesized a series of mixed-halogen compounds $CrSBr_{1-x}Cl_x$ with $x = 0$–0.67 (from now on referred to as "Cl−x") using the chemical vapor transport approach (see Experimental Section for details). The crystal structure of each compound was determined through single-crystal X-ray diffraction (SCXRD) (**Figure 3**A and Table S2, Supporting Information). Within the examined compositional range, the mixed-halogen alloys are isostructural to the parent compound CrSBr with the space group $Pmmn$ (Figure 3A). Because Cl is smaller than Br, Cl alloying has a significant impact on the lattice parameters, causing the lattice to "accordionize" along the a-axis, resulting in a decrease of the a- and c-lattice parameters with no significant change to the b-axis (Figure 3B and Figure S16, Supporting Information). The incompressibility of the structure along the b-axis stems from the Cr—(Cl/Br) bonds lying parallel to the ac-plane. At the highest Cl content (Cl-67), the a- and c-axes have compressed by 2.2% and 4.9%, respectively, compared to CrSBr, with the a-axis compression exceeding the effects of pressure at 1.5 GPa (Figure S12, Supporting Information). We note that despite the structural changes resulting from Cl alloying, the crystals with the highest concentration of Cl remain exfoliatable down to the monolayer limit (Figure S17, Supporting Information).

The chemical compositions of all new materials were determined through a combination of refining the Cl/Br occupancy on the mixed anion site on SCXRD data and energy dispersive X-ray spectroscopy (EDX) (Figure 3C, Figures S18–S23, and Table S3, Supporting Information). The percentages of Cl atoms substituted on the Br sites are close to the nominal stoichiometric amount of bromine and chlorine used in the synthesis (Figure 3D). Importantly, the chemical composition maps measured using EDX (Figure 3C and Figures S18–S23, Supporting Information) show no evidence of Cl or Br clustering on the micron scale. Polarized Raman spectroscopy on all alloys supports this, demonstrating a continuous frequency increase of characteristic CrSBr modes with increasing Cl concentration (Figure S24, Supporting Information), consistent with the homogeneous substitution of the lighter Cl atoms on Br sites.[23] Despite the significant structural changes upon Cl alloying, photoluminescence measurements on the various compositions show negligi-

ble changes in the optical band gap (Figure 3E). This is consistent with previous band-structure calculations for CrSBr and CrSCl monolayers[24] and establishes our ability to tune the lattice and (as will be seen below) magnetic structure without significantly changing the electronic structure. Given the strong coupling between magnetism and optical and electronic properties in CrSBr, Cl alloying offers an entirely new space for designing magneto-optical and magneto-electronic properties without drastically affecting the band structure.

We now turn to explore how the magnetic properties of the mixed-halogen compounds change with increasing Cl content. In **Figure 4**A, we plot χ versus T for all compounds. For Cl concentrations up to Cl-41, we observe a clear AFM transition with a peak in χ at T_N, followed by a decrease in χ at low T with no difference between zero-field-cooled (ZFC) and field-cooled (FC) traces. T_N for each stoichiometry up to Cl-41 was extracted numerically by finding the zero-crossings in $d\chi/dT$ (Figures S25 and S26, Supporting Information) and is found to decrease linearly at a rate of $dT_N/dx = -61.8$ K x^{-1} (inset of Figure 4A). The corresponding Curie–Weiss analysis (Figure S27, Supporting Information) for this compositional range reveals that θ_W also decreases with increasing Cl content while the Curie constant remains constant, indicating a weakening of the intralayer FM coupling without a change in the $S = {}^3/_2$ Cr^{3+} moments.

At high T, Cl-57 and Cl-67 follow a similar trend to the lower Cl concentrations. Specifically, θ_W lowers with increasing Cl content. Near the magnetic ordering temperature, however, the χ of Cl-57 and Cl-67 show distinctly different behavior from the lower Cl concentrations. For both compounds, the χ versus T traces display a small kink (at $T = 100$ and 86 K for Cl-57 and Cl-67, respectively), a broad maximum (at $T = 89$ and 42 K), and a clear divergence between the FC and ZFC traces at low T. These features suggest the possibility of multiple magnetic phase transitions, and further indicate that the magnetic ground state of Cl-57 and Cl-67 cannot be described as a trivial antiferromagnet (Figure S26, Supporting Information for additional axial orientations). Complementary ac magnetic susceptibility measurements on Cl-57 and Cl-67 at zero dc field confirm the presence of multiple magnetic transitions and reveal frequency-dependent behavior (Figures S28 and S29, Supporting Information), suggesting these compounds are best described as spin glasses or glassy magnets. We hypothesize the glassiness emerges either from intralayer magnetic disorder or from competing FM and AFM interlayer interactions (see discussion below). Regardless, the magnetic critical temperatures (identified by peaks in the in-phase magnetic susceptibility) follow the same trend as the lower Cl concentrations (Figures S27–S29, Supporting Information for details). This indicates that, over the entire compositional range, increased Cl alloying leads to decreased magnetic ordering temperatures and weakened intralayer coupling.

To better understand the origin of this unusual magnetic behavior at high Cl content, we performed axial-oriented M versus $\mu_0 H$ traces at 2 K for each stoichiometry (Figure 4B–D). For $\mu_0 H$ along the easy b-axis (Figure 4C), we observe a clear AFM-to-FM spin-flip transition for Cl doping up to Cl-41. The H_{SAT}, which we define as the midpoint of the transition where $M = 0.5$ M_{SAT} to better illustrate the transition at higher Cl concentrations, decreases sharply with increasing Cl content, indicating a weakening of the interlayer AFM coupling. For Cl-57
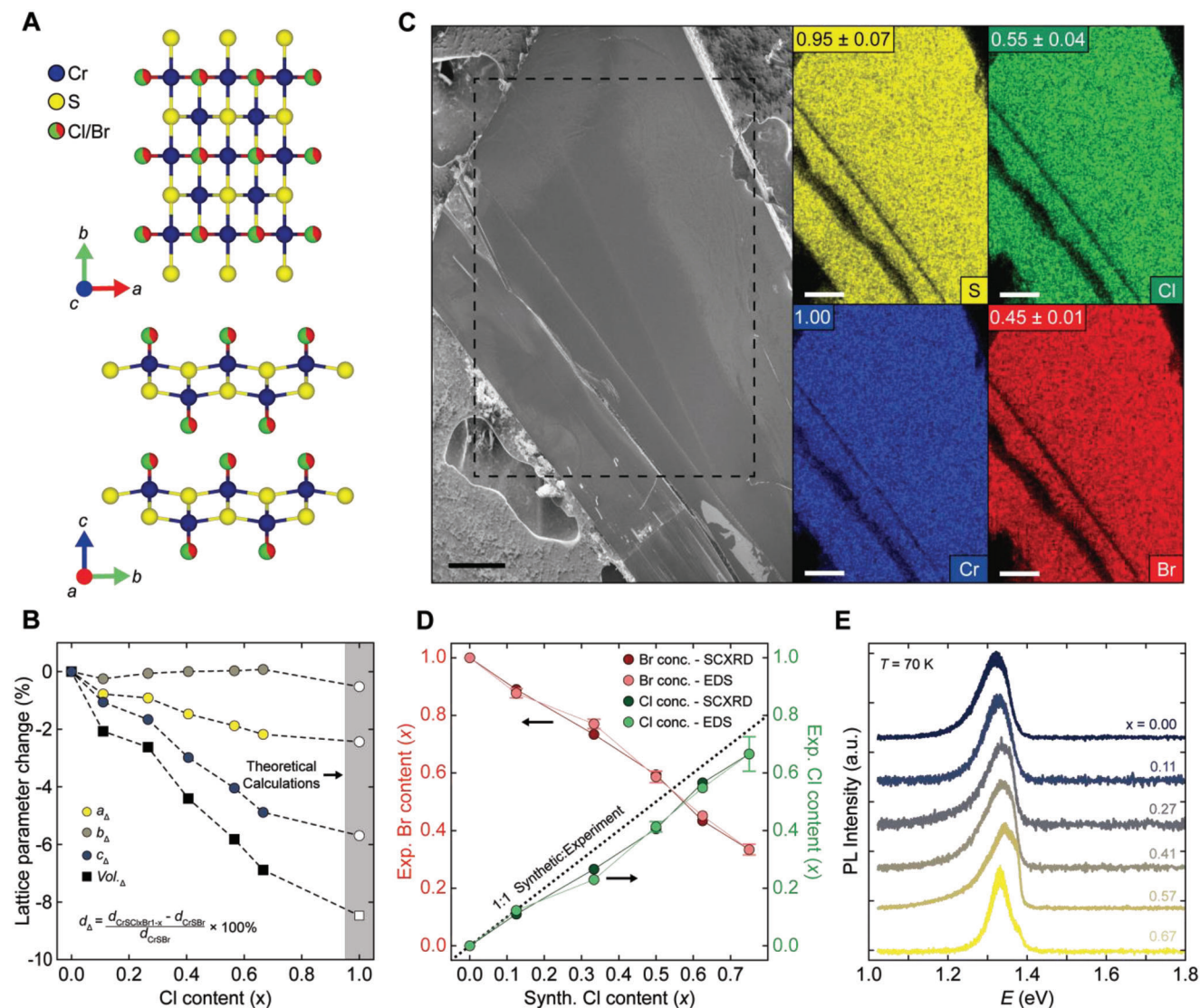
**ADVANCED
SCIENCE NEWS**

www.advancedsciencenews.com

**ADVANCED
PHYSICS
RESEARCH**
Open Access

www.advphysicsres.com

Figure 3. Structural parameters and electronic properties of CrSBr$_{1-x}$Cl$_x$. A) Crystal structure of Cl-57 as viewed along the c-axis (top) and a-axis (bottom). B) Lattice parameter ratio versus Cl content (x) for CrSBr$_{1-x}$Cl$_x$. C) Left: scanning electron microscopy (SEM) image of a cleaved crystal of Cl-57. Right: corresponding EDX elemental mapping. Blue, yellow, red, and green maps correspond to Cr, S, Br, and Cl elemental mapping, respectively. In each elemental map, the top-left inset shows the average concentration relative to Cr. The error bar is the standard deviation between multiple measurements and crystals. In all images, the scale bar is 100 μm. D) Halogen content determined using SCXRD and EDX versus Cl content used in chemical vapor transport reactions. The dashed black line demarcates 1:1 measured Cl content to Cl content used in chemical vapor transport reactions. E) Photoluminescence intensity versus photon energy for all synthesized Cl concentrations. The corresponding Cl content for each trace is given in the inset. All data were taken at 70 K.

and Cl-67, we observe s-shaped M versus $\mu_0 H$ traces with no observable hysteresis. We propose that this change in behavior arises from competing interlayer FM Cr–Cl–Cl–Cr interactions and AFM Cr–Br–Br–Cr interactions. In the aggregate, this leads to a negligible interlayer coupling for Cl-57 and Cl-67, and causes these two compositions to behave as ferromagnets under small applied fields. For $\mu_0 H$ along the a- and c-axes (Figure 4B,D, respectively), all alloys display similar behavior—a continuous spin canting process whereby the b-axis aligned spins cant toward the applied field direction. We observe a reduction in a- and c-axis H_{SAT}, defined as the point where $M = 0.9\ M_{SAT}$, signifying a lowering of the magnetic anisotropy energy. A summary of the

dependence of all axial saturation fields on Cl doping is given in the bottom inset of Figure 4A. Remarkably, the a- and b-axis H_{SAT} approach zero, indicating a diminishing anisotropy between the two in-plane directions, while the out-of-plane anisotropy only decreases by ≈50% (see also Figure S30, Supporting Information for a detailed comparison between CrSBr and Cl-57). This reduction in the effective anisotropy between the a- and b-axes motivates further study of the critical behavior of these high Cl-content materials, specifically the possibility that they could display 2D-XY behavior at the monolayer limit.[4c,25]

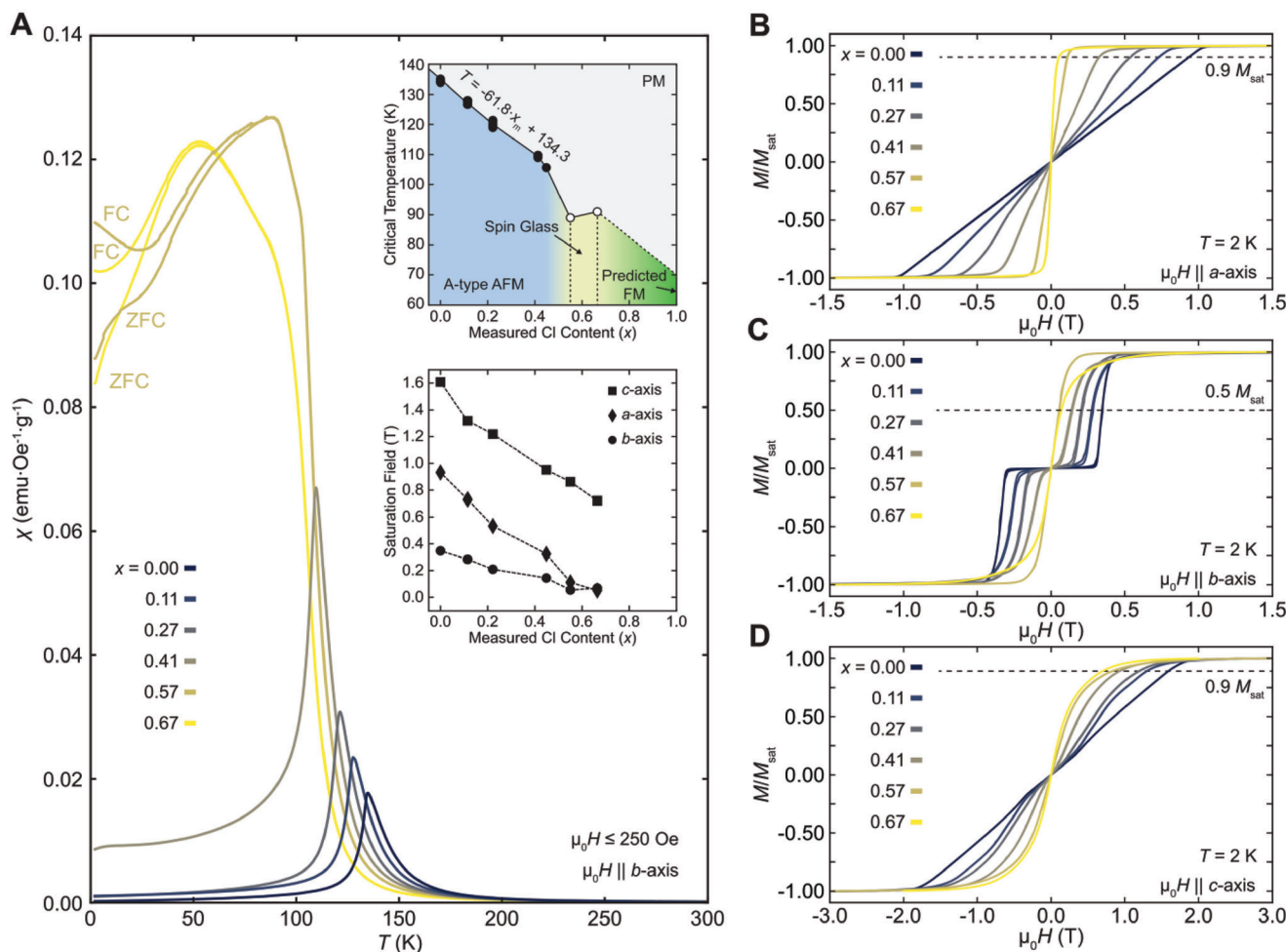The large unit cells needed to adequately model random distributions of halogens in the alloys precluded detailed

Figure 4. Magnetic properties of $CrSBr_{1-x}Cl_x$. A) χ versus T for various Cl contents (x). A measuring field of 250 Oe was used for Cl-00, Cl-11, and Cl-27, whereas a measuring field of 100 Oe was used for Cl-41, Cl-57, and Cl-67. For Cl-00, Cl-11, Cl-27, and Cl-41, only the zero-field trace is shown as it overlaps the field-cooled trace. For Cl-57 and Cl-67, both zero-field-cooled and field-cooled traces are shown. The top inset shows extracted critical temperature versus Cl content. Gray, blue, and yellow regions correspond to experimentally identified PM, AFM, and spin-glass regions, respectively. The green region corresponds to the predicted FM state for CrSCl (Table S4, Supporting Information). Up to Cl-41, the critical temperature depends linearly on Cl doping. The linear fit parameters are given in the inset. The bottom inset shows the extracted saturation magnetic fields at 2 K for fields parallel to the a-, b-, and c-axes. M normalized to the saturation magnetization (M/M_{SAT}) versus $\mu_0 H$ at 2 K for $\mu_0 H$ oriented along the B) a-, C) b-, and D) c- axes. The saturation magnetic field is defined as the magnetic field when the magnetization is 90%, 50%, and 90% of the saturation magnetization for the a-, b-, and c-axes, respectively.

computational studies of specific compositions. Instead, we modeled the magnetic properties of the theoretical end-member of this series, CrSCl, to better understand the experimental trends. Because CrSCl is not currently experimentally accessible, we simulated and relaxed the structure using CrSBr as a model lattice (Figure S31 and Table S4, Supporting Information). The relaxed CrSCl structure agrees remarkably well with an extrapolation of the experimental data up to 100% Cl content (Figure 3B and Table S4, Supporting Information).

As with the high-pressure data above, the combination of experimental magnetic data and computed magnetic and structural parameters allows us to derive magneto-structural correlations for halogen alloying in CrSBr. Increasing Cl content leads to a reduction in the interlayer spacing (Figure 3B), which could naively be expected to strengthen the interlayer magnetic exchange. Our experimental data, however, reveal that the inter-

layer coupling weakens with increasing Cl content (Figure 4C). This behavior can be explained by the reduced orbital overlap of interlayer Cr–Cl–Cl–Cr exchange compared to Cr–Br–Br–Cr. Consistent with this hypothesis, calculations predict a change in the interlayer coupling from AFM in CrSBr to FM in CrSCl (Table S4 and Figure S31, Supporting Information), confirming that orbital overlap between the halogens across the vdW gap, rather than the interlayer Cr–Cr distance is responsible for directing the sign and strength of interlayer exchange. These results support the conclusion that the glassy behavior of Cl-57 and Cl-67 arises from competing interlayer FM Cr–Cl–Cl–Cr and AFM Cr–Br–Br–Cr interactions. We note that the change in sign of the interlayer coupling upon Cl substitution in CrSBr is distinctly different from what is observed in bulk chromium trihalides, where the interlayer coupling is always AFM in the high-T monoclinic structure and FM in the low-T rhombohedral structure,

**ADVANCED
SCIENCE NEWS**

www.advancedsciencenews.com

**ADVANCED
PHYSICS
RESEARCH**

Open Access

www.advphysicsres.com

independent of the identity of the halide.[25] The weak interlayer coupling emerging from competing FM and AFM interactions in Cl-57 and Cl-67 should make the magnetic ground state in these materials particularly susceptible to external stimuli, such as strain, pressure, and magnetic field, making exfoliated flakes of these materials promising candidates for switchable 2D devices.

The largest change in the calculated intralayer coupling upon Cl substitution is the magnitude of J_1, which decreases by $\approx 80\%$ while remaining FM (Table S4, Supporting Information). The shorter calculated d_{Cr-Cr} in CrSCl compared to CrSBr should increase the contributions of AFM direct exchange, though this is unlikely to fully explain the marked drop in the magnitude of the exchange energy. While the Cr—S_2—Cr and Cr—X—Cr bond angles associated with J_1 do change with halogen substitution (Figure S16 and Table S4, Supporting Information), the large reduction in the superexchange contribution to J_1 is most likely driven by the more ionic nature of the Cr—Cl bond compared to the more covalent Cr—Br bond. This predicted decrease in J_1 for CrSCl compared to CrSBr explains a majority of the reduction in θ_W with increasing Cl content. However, examination of the other exchange pathways is useful to better distinguish the relative contributions of structural and electronic changes on magnetism, in addition to the relative effects of direct exchange and superexchange.

Because Cl substitution induces an expansion along the *b*-axis, the reduced magnitude of J_3 cannot be explained by direct exchange, and must instead be rationalized by the shift in the Cr—S_1—Cr bond angle toward 180°, which enhances the AFM contributions in the superexchange pathway (Table S4 and Figure S16, Supporting Information). Similarly, because Cl substitution has little effect on the d_{Cr-Cr} relevant to J_2, direct exchange is unlikely to contribute strongly to changes in J_2. Surprisingly, while J_2 is calculated to become more strongly FM, the Cr—S—Cr bond angles relevant to J_2 increase away from 90° (Table S4, Supporting Information), suggesting that electronic, rather than structural modifications, must drive the changes in magnetic exchange. Here, we propose that the reduced covalency of the Cr–Cl interaction (compared to Cr–Br) leads to an increase in the Cr—S bond covalency (indicated by a reduction in d_{Cr-S2}), which enhances the magnitude of the J_2 superexchange. Further, this change in the Cr–halogen covalency helps explain the changes in magnetic anisotropy with Cl substitution. Our experimental and computational data support large reductions in the magnetic anisotropy energy when Cl is substituted for Br (Table S4, Supporting Information), in line with previously predicted results.[22] The combined effects of reduced Cr–halogen covalency and smaller spin–orbit coupling for Cl compared to Br should dramatically weaken magnetocrystalline anisotropy in these materials, which is largely derived from anisotropic exchange interactions mediated by the halogens.

Intriguingly, a comparison of the Curie-Weiss analyses performed at the highest pressure (1.39 GPa—Figure S5, Supporting Information) and at the highest Cl substitution (Cl-67—Figure S27, Supporting Information) reveals nearly identical changes in the θ_W, implying similar changes in the overall magnitude of the intralayer FM exchange. However, the effects on the magnetic ordering temperature are much more dramatic for Cl substitution (−43.5 K vs CrSBr) compared to pressure (−16.6 K at 1.39 GPa vs ambient P), indicating that other factors play a key role in

the magnetic ordering temperature of CrSBr and its analogs. The presence of interlayer frustration in the Cl-substituted compounds may partly explain the reduced critical temperatures, but the small magnitude of interlayer exchange compared to the intralayer exchange suggests this effect should play a small role in dictating the ordering temperature. Instead, we propose that the reduced magnetic anisotropy between the *a*- and *b*-axes in the alloys suppresses the magnetic ordering temperature. An intermediate magnetic regime with short-range FM correlations has been observed previously in CrSBr, and these results could support claims that this regime hosts 2D-XY-like behavior (Figure S32, Supporting Information),[14f,g] motivating further study of the magnetism of the mixed-halogen compounds at the 2D limit. More broadly, the effects of anisotropy observed here indicate that strong uniaxial anisotropy is required to maximize magnetic ordering temperatures for in-plane, orthorhombic 2D magnets and that 2D-XY-like magnetic regimes may be accessible outside of materials with high rotational symmetry.

3. Conclusion

In summary, we have demonstrated two routes to tune the magnetic properties of the layered semiconductor CrSBr: pressure and halogen substitution. Compression of the lattice under pressure reduces T_N through the suppression of intralayer FM interactions and increases all axial saturation fields due to an increase in interlayer exchange energy. Cl alloying similarly decreased T_N, due to the suppression of intralayer FM coupling through anisotropic lattice compression and reduced Cr–halogen covalency. However, a key difference with Cl-alloying is the observed *decrease* in all axial saturation fields which results from *decreasing* interlayer exchange energy and magnetic anisotropy. Preliminary optical and exfoliation experiments indicate that these Cl-substituted analogs retain the semiconducting properties and ambient stability of the parent CrSBr phase, motivating further characterization of the coupling between magnetism and optical, electronic, and structural properties across the series. More generally, these results highlight that the CrSBr family of 2D magnets offers the ability to chemically or mechanically control magnetic coupling and anisotropy, similar to the more thoroughly studied chromium trihalide family. While the achievable Cl-alloying range in our study was relatively large, chalcogen and iodine alloys were found to be synthetically inaccessible with CVT. Synthesizing these compounds will require the development of new synthetic methods, but we predict they will expand upon the rich phase space of these materials, which includes diverse magnetic ground states (FM, AFM, spin glass) and spans a wide range of ordering temperatures. Furthermore, the enhanced tunability of the interlayer coupling, improved stability in ambient conditions, and semiconducting transport properties strongly motivate the incorporation of CrSBr and its analogues into functional 2D spintronic devices.

4. Experimental Section

Synthesis of CrSBr: Large single crystals of CrSBr were grown using a chemical vapor transport reaction described in ref. [14g].

Synthesis of CrSBr$_{1-x}$Cl$_x$:   The synthesis of Cl-alloyed CrSBr was achieved using a modified reaction of the pure CrSBr reaction. Chromium

Table 1. Ratio of reagents for each particular Cl-alloyed CrSBr sample.

Target composition	$Cr:S:CrCl_3:CrBr_3$ target ratio	Single crystal composition
CrSBr	2/3:1:0:1/3	CrSBr
$CrSCl_{1/8}Br_{7/8}$	2/3:1:1/24:7/24	$CrSCl_{0.11}Br_{0.89}$
$CrSCl_{1/3}Br_{2/3}$	2/3:1:1/9:2/9	$CrSCl_{0.27}Br_{0.73}$
$CrSCl_{1/2}Br_{1/2}$	2/3:1:1/6:1/6	$CrSCl_{0.41}Br_{0.59}$
$CrSCl_{5/8}Br_{3/8}$	2/3:1:5/24:1/8	$CrSCl_{0.57}Br_{0.43}$
$CrSCl_{3/4}Br_{1/4}$	2/3:1:1/4:1/12	$CrSCl_{0.67}Br_{0.33}$

Note: All compositions were synthesized through chemical vapor transport (CVT) reactions using a stoichiometric amount of chromium(III) bromide/chloride, sulfur, and chromium. CVT reactions rely on all the elements having large enough partial pressures for effective mass transport through the formation of volatile transport effective species which were generated in situ at the crystal growth temperatures (850–950 °C). The temperatures used in the synthesis allowed for both halogens species to transport effectively and be incorporated into the final product; though, the final composition of the product was typically deficient in chloride (i.e., the nominal ratio of chlorine to bromine used in the synthesis was greater than the ratio derived from SCXRD and EDX). CVT reactions with higher chlorine concentrations were attempted though only resulted in the deposition of $Cr(Cl/Br)_3$ and Cr_2S_3 phases on the sink side limiting the highest chlorine alloy level to Cl-67. Note that the original synthesis[26] for Cl-alloyed CrSBr required the use of S_2Cl_2 and S_2Br_2. Because these reagents are liquid, using the original method limits the precise control of the stoichiometry compared to solids which can be mass accurately. Additionally, the original synthesis incorporated only 1/3 Cl onto the Br sites while the method described in this work can incorporate double the amount of Cl.

metal (99.94%, −200 mesh, Alfa Aesar), sulfur pieces (99.9995%, Alfa Aesar), chromium(III) chloride (anhydrous, 99.9%, Thermo Scientific), and bromine (99.99%, Aldrich) were used as received. Chromium(III) bromide was synthesized as described in ref. [14g]. In a typical reaction, a slightly off stoichiometric ratio of the reagents with a total mass of 1 g (see **Table 1** for the ratio of reagents for each particular Cl-alloyed CrSBr sample) were loaded into a 12.7 mm o.d., 10.5 mm i.d. fused silica tube which was sealed to a length of 20 cm. The tube was subjected to the following heating profile using a computer-controlled two-zone horizontal tube furnace: *Source side*: Heat to 800 °C in 24 h, soak for 48 h, heat to 875 °C in 12 h, soak for 72 h and then water quench. *Sink side*: Heat to 875 °C in 24 h, soak for 48 h, heat to 800 °C in 12 h, soak for 72 h and then water quench. *Caution!* When quenching the reaction, ensure proper PPE is used, including a full-face shield, fire-resistant lab coat, and a blast shield.

Powderization of CrSBr Crystals for Magnetometry Measurements under Pressure: CrSBr was powderized through the following process: large crystals of CrSBr were placed in a thin porcelain crucible along with enough liquid N_2 to fully submerge the crystals. The crystals were ground with a thermally equilibrated pestle for 5 min. The material was rinsed with acetone to remove residual moisture from condensation.

Determination of Applied Hydrostatic Pressure for Magnetometry Measurements under Pressure: Since the superconducting critical temperature (T_C) of Pb is well-known to linearly depend upon the applied pressure at a rate of $dT_C/dP = 0.379$ K GPa^{-1},[27] the measured T_C of Pb can be used to determine the applied pressure on CrSBr. The Pb plus CrSBr sample was first zero-field cooled below the transition to 6 K, then the magnetic susceptibility (χ) versus temperature (T) was measured with a small measuring field of 5 Oe (such that the measuring field is much less than the zero-temperature upper critical field,[28] which for lead is 800 Oe). χ versus T was measured at a rate of 0.05 K min^{-1} to ensure the transition was precisely resolved and traces with increasing and decreasing T were measured to check for measurement precision. The Pb T_C was extracted by finding the condition where $\chi = 0.5 \chi_N$ (where χ_N is the susceptibility in the normal state) and correlated to the measured pressure-cell compression.

Vibrating Sample Magnetometry under Pressure: All vibrating sample magnetometry was conducted on a Quantum Design PPMS DynaCool sys-

tem using the commercially available HMD high-pressure cell. Multiple single CrSBr crystals were selected, and powderized in liquid nitrogen using a mortar and pestle. Before and after the VSM measurements, PXRD was used to confirm there was no significant change in structure upon powderizing or after applying maximum pressure. The powder was then combined with Daphne 7373 oil and a ≈1–2 mm long wire of Pb in a Teflon capsule was inserted into the pressure cell. The variable temperature scans and field-dependent magnetic susceptibility curves for each pressure were measured during the same measurement cycle. The measurements performed at different pressures were done sequentially with increasing pressure (from zero applied pressure up to the maximum achievable pressure). After the final maximum pressure measurement, the capsule containing the CrSBr powder, Daphne 7373 oil, and the Pb manometer was removed, fixed to a brass paddle with GE varnish, and re-measured as a consistency check of the zero-pressure measurement.

Vibrating Sample Magnetometry on $CrSBr_{1−x}Cl_x$: All vibrating sample magnetometry was conducted on a Quantum Design PPMS DynaCool system. For each stoichiometry, a pristine single $CrSBr_{1−x}Cl_x$ crystal was selected and attached to a quartz paddle using GE varnish (which was cured at room temperature under ambient conditions for 30 min) and oriented with the *a*-, *b*-, or *c*-axis parallel to the applied field direction. The same crystal was used for all axial-orientated measurements. The variable temperature scans and field-dependent magnetic susceptibility curves for each axis were measured during the same measurement cycle. Between axial-oriented measurements, the crystal was removed using a 1:1 ethanol/toluene solution, dried in air, and then reoriented and reattached using GE varnish.

Ac Magnetometry on $CrSBr_{1−x}Cl_x$: All ac magnetometry was conducted on a Quantum Design PPMS DynaCool system with the ACMSII module. For each measured stoichiometry, a pristine single $CrSBr_{1−x}Cl_x$ crystal was selected and attached to a quartz paddle using GE varnish (which was cured at room temperature under ambient conditions for 30 min) and oriented with the *a*- or *b*-axis parallel to the applied magnetic field. An ac magnetic field excitation of 4 Oe was used for all measurements. The variable temperature and frequency-dependent magnetic susceptibility curves for each axis were measured during the same measurement cycle.

Ambient-Pressure Powder X-Ray Diffraction: Powder diffraction patterns were collected on a Malvern Panalytical Aeris diffractometer with a Cu Kα X-ray source energized to 40 kV and 15 mA. The X-ray beam was filtered with a Niβ filter. The LN-powderized sample of CrSBr was mounted on a Si-zero background holder which was spun during the collection to reduce preferred orientation.

Single-Crystal X-Ray Diffraction: Single crystal diffraction measurements were collected on $CrSBr_{1−x}Cl_x$ crystals using an Agilent Supernova single-crystal diffractometer. The crystals were mounted onto a MiTeGen MicroLoops holder with paratone oil. The X-ray source was a Mo Kα micro-focus energized to 50 kV and 0.8 mA. The collection temperature was maintained at 250 K using an Oxford instruments nitrogen cryostat. The data collection, integration, and reduction were performed using the Crysalis-Pro software suite. The crystal structure was solved and refined using ShelXT[29] and ShelXL[30] respectively.

Details of Diamond Anvil Cell (DAC) Assembly: Boehler–Almax diamond anvils with 300 µm culets set in tungsten carbide seats with a conical aperture of 80° were used. The anvils and seats were loaded into DacTools iBX-80 type cells. A stainless-steel gasket with a starting thickness of 250 µm was pre-indented to a thickness of ≈40 µm. A sample space with a diameter of ≈200 µm was then created in the center of the indented gasket via electro-discharge machining using a Boehler µDrill with a copper wire electrode.

High-Pressure Powder X-Ray Diffraction Measurements: To reduce texture effects in powder X-ray diffraction measurements, single crystals of CrSBr were first cooled to 77 K in liquid nitrogen and then ground with a mortar and pestle. The resulting powder was sieved to remove large, unground crystals. The sieved powder was further ground between two glass slides prior to loading in the diamond anvil cell.

The sample chamber prepared as described above was loaded with CrSBr powder, a small piece of gold foil to serve as a pressure calibrant during diffraction measurements, and two ruby microspheres (BETSA) to

**ADVANCED
SCIENCE NEWS**

www.advancedsciencenews.com

**ADVANCED
PHYSICS
RESEARCH**

Open Access

www.advphysicsres.com

serve as a pressure calibrant during gas loading. A representative photograph of one of the loaded cells is shown in Figure S11 (Supporting Information). The cell was subsequently loaded with neon as the pressure transmitting medium using the COMPRES gas loading system as GSE-CARS, at the Advanced Photon Source at Argonne National Laboratory.[31]

High-pressure powder X-ray diffraction experiments were conducted at beamline 16-ID-B, within HPCAT at the Advanced Photon Source (APS). High-intensity monochromatic synchrotron radiation with a fixed wavelength of 0.406626 Å was used as the source in all diffraction measurements. The cell was loaded into a diaphragm gas membrane assembly, which enables diffraction measurements over very small pressure increments (≈0.1 GPa). At each pressure step, separate diffraction images were collected without rotation on the CrSBr sample and the Au foil to enable the determination of lattice parameters and sample-space pressure, respectively. Diffraction images were masked and integrated using the Dipotas 0.5.1 software package to produce the corresponding 1D diffraction patterns.[32]

Analysis of Powder X-Ray Diffraction Data: For each pressure step, the cell pressure was obtained by comparison of the lattice parameters of the Au foil with the established equation of state.[33] Powder X-ray diffraction data were then analyzed using the GSAS-II software package.[34] Due to the weak intensity of the $(00l)$ reflections and the possible overlap of the (011) and (002) reflections, it was observed that lattice parameters obtained using the Pawley method were highly sensitive to the initial parameters used in the refinement. To obtain reasonable initial parameters, the estimated b-lattice parameter was extracted by inspection of the (020) reflection, and subsequently a- and c-lattice parameters were estimated by inspection of the (110) and (011) reflections, respectively. Using these lattice parameters as the initial values, then the patterns were fit over the 2θ range 3–23° using the Pawley method to extract accurate unit cell parameters at each pressure. It was noted that it was necessary to constrain the b-axis lattice parameter during initial refinements of the background, line shape, and a- and c-axis lattice parameters to obtain reasonable fits of the (020) reflection.

Then the software package EoSFit7[34] was used to fit the unit cell volume as a function of pressure. A third-order Birch–Murnaghan equation of state was used to fit the data:[35]

$$P\,(V) = \frac{3B_0}{2}\left(\left(\frac{V_0}{V}\right)^{\frac{7}{3}} - \left(\frac{V_0}{V}\right)^{\frac{5}{3}}\right)\left\{1 + \frac{3}{4}\left(B_0' - 4\right)\left(\left(\frac{V_0}{V}\right)^{\frac{2}{3}} - 1\right)\right\} \quad (1)$$

where P is the pressure, V is the unit cell volume, V_0 is the initial unit cell volume at ambient pressure, B_0 is the bulk modulus, and B_0' is the derivative of the bulk modulus with respect to pressure. A single equation of state was sufficient to fit the data at room temperature up to 3.5 GPa, suggesting no phase transition occurs in the pressure range where magnetic analyses were performed. A small anomaly was possibly observed in the b-axis lattice parameters near 0.6 GPa, though this anomaly was attributed to the necessary constraints applied to the b-axis lattice parameter during refinements, as described above.

Scanning Electron Microscopy: Scanning electron micrographs were collected on a Zeiss Sigma VP scanning electron microscope (SEM) using a beam energy of 5 kV. Energy dispersive X-ray spectroscopy (EDX) of the CrSBr crystals was performed with a Bruker XFlash 6|30 attachment. Spectra were collected with a beam energy of 15 kV. Elemental compositions and atomic percentages were estimated by integrating under the characteristic spectrum peaks for each element using Bruker ESPRIT 2 software.

Raman Spectroscopy: Raman spectroscopy for all $CrSBr_{1-x}Cl_x$ single crystals was performed under ambient conditions in a Renishaw InVia micro-Raman microscope using a 532 nm wavelength laser. A 50× objective was used with a laser spot size of 2–3 μm. A laser power of ≈2 mW was used with a grating of 2400 g mm⁻¹ for all spectra. An acquisition time of 20 s was used for each measurement. For each crystal, 5 independent spectra were acquired and averaged after subtracting a dark background. The dark background was a spectrum acquired with no laser excitation and the same acquisition parameters.

Photoluminescence (PL) Spectroscopy: PL measurements were carried out with a 450-nm continuous-wave (CW) laser with a power of 900 μW. The PL spectra were collected by a Princeton Instruments PyLoN-IR detector cooled with liquid nitrogen. All samples were prepared by exfoliating single crystals of $CrSBr_{1-x}Cl_x$ onto SiO_2/Si+ substrates passivated with 1-dodecanol. The exfoliation was done under inert conditions in an N_2 glovebox with < 1 ppm O_2 and < 1 ppm H_2O content. Thin-bulk flakes were identified by optical microscopy and loaded into an Oxford Instruments Microstat HiRes2 cryostat inside the glovebox to avoid exposing the samples to air before measurements.

Exfoliation: $CrSBr_{1-x}Cl_x$ flakes were exfoliated onto 285 nm SiO_2/Si+ substrates using mechanical exfoliation with Scotch Magic tape.[36] Before exfoliation, the substrates were cleaned with a gentle oxygen plasma to remove adsorbates from the surface and increase flake adhesion.[37] The exfoliation was done under inert conditions in an N_2 glovebox with <1 ppm O_2 and <1 ppm H_2O content. Flake thickness was identified using optical contrast and then confirmed with atomic force microscopy.

Atomic Force Microscopy: Atomic force microscopy was performed in a Bruker Dimension Icon using OTESPA-R3 tips in tapping mode. Flake thicknesses were extracted using Gwyddion to measure histograms of the height difference between the substrate and the desired flake.

Theoretical Calculations: Ab initio calculations of bulk CrSBr and CrSCl were performed using DFT implemented in the QUANTUM ESPRESSO package.[38] Norm-conserving pseudopotentials with a plane-wave energy cutoff of 85 Ry were employed. For structural optimization, the spin-polarized Perdew–Burke–Ernzerhof exchange-correlation functional was employed, with dispersion corrections within the D2 formalism[39] (PBE-D2) included to account for the vdW interactions. The structures were fully relaxed until the force on each atom was < 0.005 eV Å⁻¹. The calculated lattice constants for bulk CrSBr and CrSCl were 3.5 and 3.4 Å along the a-axis, respectively, and both 4.7 Å along the b-axis. The calculated interlayer distance for bulk CrSBr and CrSCl were 8 and 7.5 Å, respectively. For each pressure applied, the intra- and interlayer Heisenberg magnetic exchange couplings J were calculated in $3 \times 3 \times 1$ and $3 \times 3 \times 2$ supercells respectively, by a four-state mapping method[40] within the local spin density approximation (LSDA). The Curie temperature was calculated using metropolis Monte Carlo (MC) methods implemented in the VAMPIRE package.[41] The critical exponent was determined by fitting the temperature-dependent normalized magnetization $m(T)$ to the Curie–Bloch equation in the classical limit $m\,(T) = \left(1 - \frac{T}{T_C}\right)^{\beta}$. The saturation fields along different axes were extracted based on the Heisenberg model $H = H_0 + H_{inter} - g\mu_B \sum_i h \cdot \mathbf{S}_i$, where $H_{inter} = \sum_{i \in t, j \in b} J_{inter,ij}\mathbf{S}_i \cdot \mathbf{S}_j$ with t and b denote the top and bottom layers in a unit cell, h represents the external magnetic field. The ground state energy differences between the FM and AFM states $(E^{FM} - E^{AFM})$ under different pressures were calculated with spin–orbit coupling (SOC) taken into account within LSDA, based on the structures revealed by PBE-D2.

Supporting Information

Supporting Information is available from the Wiley Online Library or from the author.

Acknowledgments

Conflict of Interest

The authors declare no conflict of interest.

Data Availability Statement

The data that support the findings of this study are available from the corresponding author upon reasonable request.

Keywords

[1] a) C. Gong, L. Li, Z. Li, H. Ji, A. Stern, Y. Xia, T. Cao, W. Bao, C. Wang, Y. Wang, Z. Q. Qiu, R. J. Cava, S. G. Louie, J. Xia, X. Zhang, *Nature* **2017**, *546*, 265; b) B. Huang, G. Clark, E. Navarro-Moratalla, D. R. Klein, R. Cheng, K. L. Seyler, D. Zhong, E. Schmidgall, M. A. McGuire, D. H. Cobden, W. Yao, D. Xiao, P. Jarillo-Herrero, X. Xu, *Nature* **2017**, *546*, 270.

[2] V. P. Ningrum, B. Liu, W. Wang, Y. Yin, Y. Cao, C. Zha, H. Xie, X. Jiang, Y. Sun, S. Qin, X. Chen, T. Qin, C. Zhu, L. Wang, W. Huang, *Research* **2020**, *2020*, 1768918.

[3] a) P. Němec, M. Fiebig, T. Kampfrath, A. V. Kimel, *Nat. Phys.* **2018**, *14*, 229; b) J. F. Sierra, J. Fabian, R. K. Kawakami, S. Roche, S. O. Valenzuela, *Nat. Nanotechnol.* **2021**, *16*, 856.

[4] a) S. Son, M. J. Coak, N. Lee, J. Kim, T. Y. Kim, H. Hamidov, H. Cho, C. Liu, D. M. Jarvis, P. A. C. Brown, J. H. Kim, C.-H. Park, D. I. Khomskii, S. S. Saxena, J.-G. Park, *Phys. Rev. B* **2019**, *99*, 041402; b) D. Weber, L. M. Schoop, V. Duppel, J. M. Lippmann, J. Nuss, B. V. Lotsch, *Nano Lett.* **2016**, *16*, 3578; c) X. Cai, T. Song, N. P. Wilson, G. Clark, M. He, X. Zhang, T. Taniguchi, K. Watanabe, W. Yao, D. Xiao, M. A. McGuire, D. H. Cobden, X. Xu, *Nano Lett.* **2019**, *19*, 3993; d) Z. Zhang, J. Shang, C. Jiang, A. Rasmita, W. Gao, T. Yu, *Nano Lett.* **2019**, *19*, 3138.

[5] a) M. Bonilla, S. Kolekar, Y. Ma, H. C. Diaz, V. Kalappattil, R. Das, T. Eggers, H. R. Gutierrez, M.-H. Phan, M. Batzill, *Nat. Nanotechnol.*

2018, *13*, 289; b) J. Li, B. Zhao, P. Chen, R. Wu, B. Li, Q. Xia, G. Guo, J. Luo, K. Zang, Z. Zhang, H. Ma, G. Sun, X. Duan, X. Duan, *Adv. Mater.* **2018**, *30*, 1801043.

[6] X. Xiao, P. Urbankowski, K. Hantanasirisakul, Y. Yang, S. Sasaki, L. Yang, C. Chen, H. Wang, L. Miao, S. H. Tolbert, S. J. L. Billinge, H. D. Abruña, S. J. May, Y. Gogotsi, *Adv. Funct. Mater.* **2019**, *29*, 1809001.

[7] a) J.-U. Lee, S. Lee, J. H. Ryoo, S. Kang, T. Y. Kim, P. Kim, C.-H. Park, J.-G. Park, H. Cheong, *Nano Lett.* **2016**, *16*, 7433; b) Y. Deng, Y. Yu, Y. Song, J. Zhang, N. Z. Wang, Z. Sun, Y. Yi, Y. Z. Wu, S. Wu, J. Zhu, J. Wang, X. H. Chen, Y. Zhang, *Nature* **2018**, *563*, 94; c) S. Y. Park, D. S. Kim, Y. Liu, J. Hwang, Y. Kim, W. Kim, J. Y. Kim, C. Petrovic, C. Hwang, S. K. Mo, H. J. Kim, B. C. Min, H. C. Koo, J. Chang, C. Jang, J. W. Choi, H. Ryu, *Nano Lett.* **2020**, *20*, 95; d) I. A. Verzhbitskiy, H. Kurebayashi, H. Cheng, J. Zhou, S. Khan, Y. P. Feng, G. Eda, *Nat. Electron.* **2020**, *3*, 460; e) K. Lee, A. H. Dismukes, E. J. Telford, R. A. Wiscons, J. Wang, X. Xu, C. Nuckolls, C. R. Dean, X. Roy, X. Zhu, *Nano Lett.* **2021**, *21*, 3511.

[8] E. J. Telford, A. H. Dismukes, K. Lee, M. Cheng, A. Wieteska, A. K. Bartholomew, Y.-S. Chen, X. Xu, A. N. Pasupathy, X. Zhu, C. R. Dean, X. Roy, *Adv. Mater.* **2020**, *32*, 40.

[9] a) E. J. Telford, A. H. Dismukes, R. L. Dudley, R. A. Wiscons, K. Lee, D. G. Chica, M. E. Ziebel, M.-G. Han, J. Yu, S. Shabani, A. Scheie, K. Watanabe, T. Taniguchi, D. Xiao, Y. Zhu, A. N. Pasupathy, C. Nuckolls, X. Zhu, C. R. Dean, X. Roy, *Nat. Mater.* **2022**, *21*, 754; b) C. Boix-Constant, S. Mañas-Valero, A. M. Ruiz, A. Rybakov, K. A. Konieczny, S. Pillet, J. J. Baldoví, E. Coronado, *arXiv* **2022**, 2204.04095; c) C. Ye, C. Wang, Q. Wu, S. Liu, J. Zhou, G. Wang, A. Söll, Z. Sofer, M. Yue, X. Liu, M. Tian, Q. Xiong, W. Ji, X. R. Wang, *arXiv* **2022**, 2205.09077; d) F. Wu, I. Gutiérrez-Lezama, S. A. López-Paz, M. Gibertini, K. Watanabe, T. Taniguchi, F. O. v. Rohr, N. Ubrig, A. F. Morpurgo, *Adv. Mater.* **2022**, *34*, 2109759.

[10] N. P. Wilson, K. Lee, J. Cenker, K. Xie, A. H. Dismukes, E. J. Telford, J. Fonseca, S. Sivakumar, C. Dean, T. Cao, X. Roy, X. Xu, X. Zhu, *Nat. Mater.* **2021**, *20*, 1657.

[11] J. Cenker, S. Sivakumar, K. Xie, A. Miller, P. Thijssen, Z. Liu, A. Dismukes, J. Fonseca, E. Anderson, X. Zhu, X. Roy, D. Xiao, J.-H. Chu, T. Cao, X. Xu, *Nat. Nanotechnol.* **2022**, *17*, 256.

[12] a) Y. J. Bae, J. Wang, A. Scheie, J. Xu, D. G. Chica, G. M. Diederich, J. Cenker, M. E. Ziebel, Y. Bai, H. Ren, C. R. Dean, M. Delor, X. Xu, X. Roy, A. D. Kent, X. Zhu, *Nature* **2022**, *609*, 282; b) G. M. Diederich, J. Cenker, Y. Ren, J. Fonseca, D. G. Chica, Y. J. Bae, X. Zhu, X. Roy, T. Cao, D. Xiao, X. Xu, *arXiv* **2022**, https://doi.org/10.1038/s41565-022-01259-1.

[13] a) O. Göser, W. Paul, H. G. Kahle, *J. Magn. Magn. Mater.* **1990**, *92*, 129; b) J. Beck, *Z. Anorg. Allg. Chem.* **1990**, *585*, 157.

[14] a) S. Chen, F. Wu, Q. Li, H. Sun, J. Ding, C. Huang, E. Kan, *Nanoscale* **2020**, *12*, 15670; b) H. Wang, J. Qi, X. Qian, *Appl. Phys. Lett.* **2020**, *117*, 083102; c) Y. Guo, Y. Zhang, S. Yuan, B. Wang, J. Wang, *Nanoscale* **2018**, *10*, 18036; d) Z. Jiang, P. Wang, J. Xing, X. Jiang, J. Zhao, *ACS Appl. Mater. Interfaces* **2018**, *10*, 39032; e) D. L. Esteras, A. Rybakov, A. M. Ruiz, J. J. Baldovi, *arXiv* **2022**, 2206.09277; f) S. A. López-Paz, Z. Guguchia, V. Y. Pomjakushin, C. Witteveen, A. Cervellino, H. Luetkens, N. Casati, A. F. Morpurgo, F. O. v. Rohr, *arXiv* **2022**, 2203.11785; g) A. Scheie, M. Ziebel, D. G. Chica, Y. J. Bae, X. Wang, A. I. Kolesnikov, X. Zhu, X. Roy, *Adv. Sci.* **2022**, *9*, 2202467.

[15] K. Yang, G. Wang, L. Liu, D. Lu, H. Wu, *Phys. Rev. B* **2021**, *104*, 144416.

[16] a) J. L. Lado, J. Fernández-Rossier, *2D Mater.* **2017**, *4*, 035002; b) B. Huang, M. A. McGuire, A. F. May, D. Xiao, P. Jarillo-Herrero, X. Xu, *Nat. Mater.* **2020**, *19*, 1276.

[17] A. C. Komarek, T. Taetz, M. T. Fernández-Díaz, D. M. Trots, A. Möller, M. Braden, *Phys. Rev. B* **2009**, *79*, 104425.

[18] J. Angelkort, A. Wölfel, A. Schönleber, S. van Smaalen, R. K. Kremer, *Phys. Rev. B* **2009**, *80*, 144416.

[19] R. W. Grant, *J. Appl. Phys.* **1971**, *42*, 1619.

[20] a) T. M. Cham, S. Karimeddiny, A. H. Dismukes, X. Roy, D. C. Ralph, Y. K. Luo, *arXiv* **2022**, 2206.01286; b) W. Liu, X. Guo, J. Schwartz, H. Xie, N. Dhale, S. H. Sung, A. L. N. Kondusamy, X. Wang, H. Zhao, D. Berman, R. Hovden, L. Zhao, B. Lv, *arXiv* **2022**, 2203.09582; c) D. J. Rizzo, A. S. McLeod, C. Carnahan, E. J. Telford, A. H. Dismukes, R. A. Wiscons, Y. Dong, C. Nuckolls, C. R. Dean, A. N. Pasupathy, X. Roy, D. Xiao, D. N. Basov, *Adv. Mater.* **2022**, *34*, 2201000.

[21] a) J. B. Goodenough, *Phys. Rev.* **1955**, *100*, 564; b) J. Kanamori, *J. Phys. Chem. Solids* **1959**, *10*, 87; c) P. W. Anderson, *Phys. Rev.* **1950**, *79*, 350.

[22] B. Xu, Shenchang, K. Jiang, J. Yin, Z. Liu, Y. Cheng, W. Zhong, *Appl. Phys. Lett.* **2020**, *116*, 0511031.

[23] a) A. McCreary, T. T. Mai, F. G. Utermohlen, J. R. Simpson, K. F. Garrity, X. Feng, D. Shcherbakov, Y. Zhu, J. Hu, D. Weber, K. Watanabe, T. Taniguchi, J. E. Goldberger, Z. Mao, C. N. Lau, Y. Lu, N. Trivedi, R. V. Aguilar, A. R. H. Walker, *Nat. Commun.* **2020**, *11*, 3879; b) Y. Zhang, X. Wu, B. Lyu, M. Wu, S. Zhao, J. Chen, M. Jia, C. Zhang, L. Wang, X. Wang, Y. Chen, T. Mei, T. Taniguchi, K. Watanabe, H. Yan, Q. Liu, L. Huang, Y. Zhao, M. Huang, *Nano Lett.* **2020**, *20*, 729; c) H. Wang, P. Lei, X. Mao, X. Kong, X. Ye, P. Wang, Y. Wang, X. Qin, J. Meijer, H. Zeng, F. Shi, J. Du, *Chin. Phys. Lett.* **2022**, *39*, 047601; d) D. R. Klein, D. MacNeill, Q. Song, D. T. Larson, S. Fang, M. Xu, R. A. Ribeiro, P. C. Canfield, E. Kaxiras, R. Comin, P. Jarillo-Herrero, *Nat. Phys.* **2019**, *15*, 1255.

[24] C. Wang, X. Zhou, L. Zhou, N.-H. Tong, Z.-Y. Lu, W. Ji, *Sci. Bull.* **2019**, *64*, 293.

[25] M. Abramchuk, S. Jaszewski, K. R. Metz, G. B. Osterhoudt, Y. Wang, K. S. Burch, F. Tafti, *Adv. Mater.* **2018**, *30*, 1801325.

[26] M. Saßmannshausen, H. D. Lutz, *Mater. Res. Bull.* **2000**, *35*, 2431.

[27] Quantum Design Japan, **2016**.

[28] G. Chanin, J. P. Torre, *Phys. Rev. B* **1972**, *5*, 4357.

[29] G. M. Sheldrick, *Acta Crystallogr. Section A Foundations Adv.* **2015**, *71*, 3.

[30] G. M. Sheldrick, *Acta Crystallogr. Section C Struct. Chem.* **2015**, *71*, 3.

[31] M. Rivers, V. B. Prakapenka, A. Kubo, C. Pullins, C. M. Holl, S. D. Jacobsen, *High Pressure Res.* **2008**, *28*, 273.

[32] C. Prescher, V. B. Prakapenka, *High Pressure Res.* **2015**, *35*, 223.

[33] O. L. Anderson, D. G. Isaak, S. Yamamoto, *J. Appl. Phys.* **1989**, *65*, 1534.

[34] B. H. Toby, R. B. Von Dreele, *J. Appl. Crystallogr.* **2013**, *46*, 544.

[35] a) F. D. Murnaghan, *Proc. Natl. Acad. Sci. U. S. A.* **1944**, *30*, 244; b) F. Birch, *Phys. Rev.* **1947**, *71*, 809.

[36] a) K. S. Novoselov, A. K. Geim, S. V. Morozov, D. Jiang, Y. Zhang, S. V. Dubonos, I. V. Grigorieva, A. A. Firsov, *Science* **2004**, *306*, 666; b) K. S. Novoselov, D. Jiang, F. Schedin, T. J. Booth, V. V. Khotkevich, S. V. Morozov, A. K. Geim, *Proc. Natl. Acad. Sci. U. S. A.* **2005**, *102*, 10451.

[37] Y. Huang, E. Sutter, N. N. Shi, J. Zheng, T. Yang, D. Englund, H.-J. Gao, P. Sutter, *ACS Nano* **2015**, *9*, 10612.

[38] P. Giannozzi, S. Baroni, N. Bonini, M. Calandra, R. Car, C. Cavazzoni, D. Ceresoli, G. L. Chiarotti, M. Cococcioni, I. Dabo, A. D. Corso, S. d. Gironcoli, S. Fabris, G. Fratesi, R. Gebauer, U. Gerstmann, C. Gougoussis, A. Kokalj, M. Lazzeri, L. Martin-Samos, N. Marzari, F. Mauri, R. Mazzarello, S. Paolini, A. Pasquarello, L. Paulatto, C. Sbraccia, S. Scandolo, G. Sclauzero, A. P. Seitsonen, et al., *J. Phys.: Condens. Matter* **2009**, *21*, 395502.

[39] S. Grimme, *J. Comput. Chem.* **2006**, *27*, 1787.

[40] H. Xiang, C. Lee, H.-J. Koo, X. Gonga, M.-H. Whangbo, *Dalton Trans.* **2013**, *42*, 823.

[41] R. F. L. Evans, W. J. Fan, P. Chureemart, T. A. Ostler, M. O. A. Ellis, R. W. Chantrell, *J. Phys.: Condens. Matter* **2014**, *26*, 103202.